Morris, J.D., Villinger, H.W., and Klaus, A. (Eds.)
Proceedings of the Ocean Drilling Program, Scientific Results Volume 205

6. A Transport-Reaction Model of the Hydrological Systems of the Costa Rica Subduction Zone[1]

Matthias Haeckel[2, 3]

ABSTRACT

Data from Ocean Drilling Program (ODP) Legs 170 and 205 have identified systems of lateral fluid flow at the Costa Rica convergent margin: (1) an aquifer of cold seawater in the oceanic crust, (2) flow of deep-sourced fluids along conduits parallel to the décollement, and (3) vertical dewatering of compacted underthrust sediments. Numerical transport-reaction models were developed to quantify the processes of these hydrological systems. The results suggest that the lateral fluid flow in the Costa Rica subduction zone is transient (i.e., not a steady-state process).

Model runs reveal that the oceanic pore water composition has been dominated by advective or diffusive connection to the lateral flow of cold seawater in the basement for the past 240 k.y. to 1 m.y. Comparing the numerical results of this study with other hydrothermal calculations also suggests that most of this water is subducted and only a small fraction is migrating upward into the overlying sediments.

High-resolution propane gas data have been collected in prism sediments at Site 1254, showing a combination of upward advection (on the order of 0.4 cm/yr) due to compaction of the subducting oceanic sediments as well as lateral fluid flow with thermogenic origin. Numerical analysis shows that the lateral dewatering in the prism sediments is dominated by episodic events: the conduit at ~220 meters below seafloor (mbsf) has been active for ~2000 yr, whereas fluids have permeated the décollement zone (~360 mbsf) for nearly 4000 yr. However, shorter fluid pulses caused by seismic activity do not seem to have much impact. Finally, the downward progressing anaerobic methane

[1] Haeckel, M., 2006. A transport-reaction model of the hydrological systems of the Costa Rica subduction zone. *In* Morris, J.D., Villinger, H.W., and Klaus, A. (Eds.), *Proc. ODP, Sci. Results,* 205, 1–26 [Online]. Available from World Wide Web: <http://www-odp.tamu.edu/publications/205_SR/VOLUME/CHAPTERS/ 215.PDF>. [Cited YYYY-MM-DD]
[2] Dalhousie University, Department of Oceanography, 1355 Oxford Street, Halifax NS B3H 4J1, Canada.
[3] Present address: Leibniz Institute for Marine Sciences, Wischhofstrasse 1-3, D-24148 Kiel, Germany.
mhaeckel@ifm-geomar.de

Initial receipt: 28 November 2005
Acceptance: 12 July 2006
Web publication: 15 September 2006
Ms 205SR-215

oxidation reaction front, which developed between methane-rich prism sediments and sulfate-rich oceanic sediments, was analyzed. The numerical simulations show that a minimum of ~15 kg C/m² is oxidized within 17 k.y. of subduction (1.5 km arcward of the deformation front), probably partially provided by methane hydrates in the prism wedge.

INTRODUCTION

At convergent margins, fluids and subducted sediments play an important role in volcanic arc magmatism and element cycling. As the oceanic plate is being subducted, sediments are compacted and minerals dehydrate (e.g., smectite-illite reaction and opal dewatering) under elevated temperature and pressure conditions, causing the release of fluids (Kastner et al., 1991). At depths >50 km, metamorphic reactions of the crust and serpentinized mantle become important fluid sources (Rüpke et al., 2002). Water-soluble elements are mobilized from subducting sediments and the oceanic basement. These fluids are then either expelled through the prism wedge into the ocean, representing a significant input source for some elements (Kastner et al., 1991), or they are transported to the arc magma source (Morris et al., 1990; You et al., 1996) while other slab material is returned to the deep mantle.

Dewatering of deep-sourced fluids through conduits in the prism wedge and along the décollement is important for mass balance calculations. There is an ongoing debate whether these fluid flow systems are permanent features or dominated by episodic fluid pulses (Bekins et al., 1995; Hensen and Wallmann, 2005; Saffer and Bekins, 1998, 1999). Here, I numerically simulate a unique data set of propane concentrations sampled at higher than usual resolution during Ocean Drilling Program (ODP) Leg 205 to better constrain the lateral and vertical dewatering flux during subduction of the oceanic Cocos plate. The numerical transport-reaction model also reveals the transient nature of the current flow system.

In addition to this subduction-induced fluid flow, the lateral flow of seawater through the oceanic crust has been reported from several sites (Kastner and Rudnicki, 2004, and references therein). Despite research efforts over the last decade, little is known about fluid and geochemical fluxes or the detailed hydrology. So far, recharge and discharge sites have only been discovered for the hydrothermal circulation system at the eastern flank of the Juan de Fuca Ridge (Fisher and Becker, 2000; Fisher et al., 2003; Giambalvo et al., 2002; Rudnicki et al., 2001). One-dimensional steady-state models have been used to estimate vertical pore water advection rates using geochemical gradients (Giambalvo et al., 2002; Richter, 1993, 1996; Rudnicki et al., 2001). In addition, lateral flow velocities within the basement aquifer on the order of 1–10 m/yr have been estimated based on regional heat flow data and seawater residence times of 15–20 k.y. The latter were inferred from strontium (Baker et al., 1991; Silver et al., 2000) and lithium isotopic data (Chan and Kastner, 2000). Whereas these studies assume a geochemical steady state, the present study shows that the data from the Cocos plate (ODP Legs 170 and 205; Kimura, Silver, Blum, et al., 1997; Morris, Villinger, Klaus, et al., 2003) clearly reflect a non-steady-state situation. This allows estimating the age of the hydrological system in the crust in addition to calculating geochemical and fluid fluxes into the overlying sediments.

In this study, my primary focus is on the investigation of the hydrological systems in the oceanic crust and the prism wedge of the Costa Rica subduction zone. Therefore, I apply numerical transport-reaction models to simulate pore water distributions of geochemical tracers representative of the different flow regimes. In particular, I present three numerical simulations of the pore water data from Legs 170 and 205 in order to (1) estimate the fluxes of water transported in these hydrological systems, (2) quantify the geochemical fluxes into the sediments, (3) constrain the duration of fluid flow in these systems, and (4) investigate the dynamics of the methane cycle during subduction by estimating the rate of anaerobic methane oxidation (AMO).

Geological Setting and Geochemical Background

At the Costa Rica convergent margin, the Cocos plate is being subducted beneath the Caribbean plate at a rate of 88 mm/yr. Biostratigraphy, seismic reflection profiles, and gamma ray logs (Kimura, Silver, Blum, et al., 1997) as well as cosmogenic ^{10}Be values (Morris et al., 2002) show that the present margin is nonaccretionary, eventually even characterized by subduction erosion (Ranero and von Huene, 2000; Vannucchi et al., 2003). ODP investigated the Costa Rica subduction zone during two cruises, Leg 170 (Kimura, Silver, Blum, et al., 1997) and Leg 205 (Morris, Villinger, Klaus, et al., 2003), drilling a transect across the southern part of the Middle America Trench (Fig. F1).

During Leg 170, Site 1039 was located on the oceanic plate, 1.7 km seaward of the deformation front, penetrating ~400 m of sediment and stopping in the top of a gabbroic sill. Sediments of the incoming plate consist of ~150 m of siliceous hemipelagic sediments overlying ~220 m of carbonate-rich pelagic sediments (Fig. F2) (Kimura, Silver, Blum, et al., 1997). Site 1040 was drilled 1.5 km arcward of the trench into the prism wedge and the complete incoming sediment sequence, finishing in a gabbro sill at 700 meters below seafloor (mbsf) (Fig. F2). The subducting oceanic sediments are significantly compacted (~33% reduction in thickness), primarily in the upper 150 m below the décollement and much less so in the carbonaceous unit (Kimura, Silver, Blum, et al., 1997). Finally, at Site 1043, ~280 m of prism and underthrust sediments were cored 0.4 km arcward of the deformation front (Fig. F2). Compaction of the incoming sediments is much less developed, and, hence, porosities are ~10% higher than at Site 1040.

During Leg 205, two prism wedge sites were revisited and adjacent holes were drilled: Sites 1254 and 1255 (Fig. F1). Only limited coring was performed (Table T1) to locate the exact depth of the lateral fluid flow systems in proximity of the décollement. At Site 1254, the décollement zone is located at 338.5–364.2 mbsf and the lithologic boundary (siliceous hemipelagic over carbonate-rich pelagic sediment) is at 360.6 mbsf (Fig. F2). The upper thrust fault zone was placed at 197–219 mbsf. At Site 1255, the base of the décollement is located at 144.08 mbsf and coincides with the lithologic boundary. This time, oceanic sediments were drilled closer to the deformation front (i.e., Site 1253, ~200 m seaward in the deepest part of the Middle America Trench). Coring started at 370 mbsf and penetrated an upper gabbroic sill, another 20 m of sediments, and 150 m into a second sill complex, finishing at a total depth of 600 mbsf (Table T1; Fig. F2).

ODP cruises identified three major hydrological systems: lateral flow of fluids (1) in the oceanic crust, (2) along the décollement, and (3) through an upper conduit within the margin wedge. The geochemi-

F1. Drilling locations and seismic profile, p. 18.

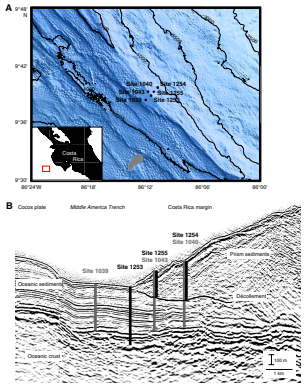

F2. Simplified lithology, p. 19.

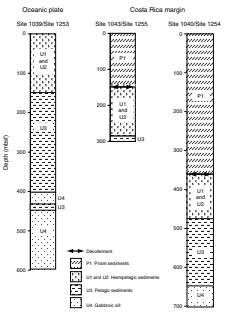

T1. Drilling locations, p. 25.

cal characteristics of the pore water are discussed below, and chemical analytics can be found in Kimura, Silver, Blum, et al. (1997) and Morris, Villinger, Klaus, et al. (2003).

Oceanic Plate Sediments

Diagenesis in the sediments of the oceanic plate (Sites 1039 and 1253; Fig. F1) is characterized by sulfate reduction degrading organic matter (OM) in surface sediments. Below the sediment surface, sulfate concentrations rapidly decrease from 27.5 to ~13 mM at 24 mbsf. Subsequently, they start to increase again, reaching seawater level at 400 mbsf, right above the first gabbroic sill (Fig. F3). Several other pore water species, such as NH_4^+, PO_4^{3-}, alkalinity, Ca^{2+}, and Sr^{2+}, follow the same trend, also returning to seawater concentrations at the base of the drilled sediment column (Fig. F3). Ammonium, phosphate, and alkalinity are produced during anoxic degradation of organic matter; hence, they rapidly increase below the sediment surface before they slowly drop back to bottom water values with increasing sediment depth. Their peaks coincide with the depth of the sulfate minimum. Methanogenesis has not been observed in the oceanic sediments. Organic carbon (C_{org}) content decreases exponentially with depth from >2 wt% at the surface to ~0.2 wt% above the sill (Fig. F4). Calcium and strontium concentrations increase with depth because of alteration and dissolution of ash layers within the sediment sequence, but below 300 mbsf both reverse back to current bottom water concentrations (Fig. F3). In addition, strontium isotope ratios return to values of modern seawater, strongly suggesting lateral flow of cold, modern seawater in the crust of the incoming plate (Kastner et al., 2000; Kastner and Rudnicki, 2004; Silver et al., 2000).

This flow of cold seawater is also believed to cool the oceanic crust, providing an explanation for the exceptionally low heat flow observed in the area (Kimura, Silver, Blum, et al., 1997; Silver et al., 2000). The average value measured over the prism wedge and the oceanic plate seaward of the trench is <30 mW/m², compared to an expected value of 100 mW/m² given the age of the oceanic crust, ~24 Ma (Langseth and Silver, 1996).

Prism and Underthrust Sediments

The prism sediments (Sites 1040, 1043, 1254, and 1255; Fig. F1) are characterized by intense sulfate reduction and subsequent methanogenesis. Between 100 and 350 mbsf this methane is bound in finely dispersed gas hydrates occupying up to 2.5% of the pore space (Hensen and Wallmann, 2005). Excess methane is diffusing across the décollement and into the sulfate-rich sediments of the incoming plate, thereby forming a downward-progressing AMO reaction front. A downward displacement of this reaction front of ~20 m with respect to the lithologic boundary (i.e., the original sediment/water interface of the oceanic sediments) is observed at Site 1040, ~1.5 km arcward of the deformation front (Kimura, Silver, Blum, et al., 1997). Closer to the deformation front at Site 1043 (0.4 km arcward), the reaction front is close to the lithological boundary and has only started to consume the sulfate in the underthrust sediments.

Two zones of lateral fluid flow have been determined in the sediments of the prism wedge (Kimura, Silver, Blum, et al., 1997): (1) along the décollement zone and (2) an upper fault zone at 200–220 mbsf.

F3. Geochemical data, Sites 1039 and 1253, p. 20.

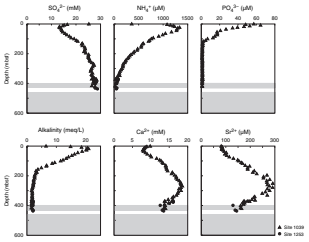

F4. Numerical model results, Sites 1039 and 1253, p. 21.

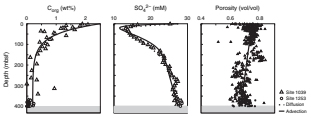

Here, distinct peaks of higher alkanes, ranging from propane to isopentane (Kimura, Silver, Blum, et al., 1997), as well as lithium (Chan and Kastner, 2000), were observed. These fluids are also enriched in Ca^{2+}, whereas other pore water constituents such as Cl^-, K^+, and Mg^{2+} show lower than seawater concentrations in these zones (Kimura, Silver, Blum, et al., 1997) (also see Fig. F5). It is well known that higher hydrocarbons are formed from organic material under elevated temperature conditions (Claypool and Kvenvolden, 1983). High pressure and elevated temperatures also favor the exchange of lithium in clay minerals (Chan and Kastner, 2000)—the transition of smectite to illite, thereby consuming K^+—as well as the dehydration of minerals (e.g., smectite-illite reaction, opal dewatering, and serpentinization). Whereas drilling causes dilution of pore water salinities due to dissociation of gas hydrates in the prism sediments, it cannot completely explain the observed chloride anomalies (Hensen and Wallmann, 2005) or the maxima of Ca^{2+} and Li^+. Hence, the occurrence of these anomalies requires fluid flow with a thermogenic origin, ~80°–150°C. Based on the thermogenic gradient, Silver et al. (2000) estimated the fluid source to be at 15–20 km depth and 40–60 km further arcward. Lithologically, these pore water excursions coincide with highly fractured intervals interpreted as fault zones and with sandy brecciated layers potentially serving as flow conduits for the deep-sourced fluid (Morris, Villinger, Klaus, et al., 2003). Closer to the trench (Sites 1043 and 1255), the flow conduit along the décollement is far less pronounced and the upper flow conduit, identified at Sites 1040 and 1254, is no longer detectable (Fig. F5).

F5. Prism and underthrust sediment pore water data, p. 22.

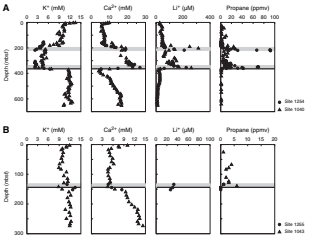

METHODS

Numerical Transport-Reaction Models

Three one-dimensional (1-D) non-steady-state transport-reaction models were developed to analyze pore water data observed at the drilling sites of Legs 170 and 205 with respect to the hydrological systems found in the basement of the oceanic plate and the prism sediments (Kimura, Silver, Blum, et al., 1997; Morris, Villinger, Klaus, et al., 2003).

As appropriate to the aim of each investigation, several dissolved chemical species (e.g., sulfate, hydrogen sulfide, ammonium, phosphate, methane, propane, lithium, and barium) were considered in these models. Numerically, this leads to a set of second-order partial differential equations of the general form (Berner, 1980):

$$\frac{\partial \phi C_i}{\partial t} = \frac{\partial}{\partial x}\left(\phi \frac{D_i}{\theta^2}\frac{\partial C_i}{\partial x} + \phi u C_i\right) + \sum R_i, \quad (1)$$

where

- ϕ = porosity,
- C_i = concentration of the dissolved chemical substance *i*,
- t = time,
- x = sediment depth,
- D_i = molecular diffusion coefficient of *i* corrected for salinity, temperature, and pressure (Li and Gregory, 1974),
- θ^2 = $1 - 2(\ln\phi)$ is the tortuosity correction for diffusion (Boudreau, 1997),

u = advective transport velocity of the solutes (positive for active upward-directed fluid flow), and
ΣR_i = all sources and sinks either producing or consuming solute i (e.g., biogeochemical reactions).

Porosity changes with depth because of compaction. An empirical relationship is used to describe such porosity changes (Boudreau, 1997):

$$\phi(x) = \phi_\infty + (\phi_0 - \phi_\infty)e^{-\beta x}, \quad (2)$$

where

ϕ_0 = porosity at the sediment surface ($x = 0$),
ϕ_∞ = porosity at infinite depth ($x = \infty$), and
β = porosity attenuation coefficient.

This equation was least-squares fitted to the observed data (Kimura, Silver, Blum, et al., 1997; Morris, Villinger, Klaus, et al., 2003), and the result was prescribed in the model runs. Equation 2 assumes steady-state compaction, which may not be completely justified in all considered model scenarios but still approximates the porosity data fairly well.

The vertical advective pore water transport has two sources, downward-directed burial modified by gravity-induced sediment compaction and active fluid flow from below:

$$u(x) = \frac{\phi_0 u_0 - \omega_\infty \phi_\infty}{\phi(x)}, \quad (3)$$

where

u_0 = active fluid flow rate at the sediment surface and
ω_∞ = sedimentation rate at infinite depth.

Because sedimentation rates did not vary much over time at the drill sites, a constant mean value is used in the calculations.

In order to significantly reduce computational costs, profiles of solid chemical compounds involved in diagenetic reactions of the solutes of interest were assumed to represent steady-state solutions. These analytical functions were least-squares fitted to the measured data, and the results were prescribed in the numerical models. Hence, only the diagenetic equations for solutes (equation 1) needed to be solved numerically. The MATLAB environment was used for this purpose. The partial differential equations (PDEs) were discretized using finite differences and a combination of Dirichlet and Neumann boundary conditions. Table T2 and the following paragraphs provide details on boundary as well as the relevant diagenetic reactions considered in the respective problem. The model parameters were adjusted manually to reproduce the measured pore water distributions as perfectly as possible.

T2. Numerical model setups, p. 26.

Model I: Diagenesis in Oceanic Plate Sediments

OM degradation in oceanic sediments primarily utilizes pore water sulfate as the terminal electron acceptor. Ammonium, phosphate, sulfide, and bicarbonate are released into the pore water along with a corresponding increase in alkalinity values:

$$(CH_2O)_a(NH_3)_b(H_3PO_4)_c + \left(\frac{1}{2}a\right)SO_4^{2-} \rightarrow \left(\frac{1}{2}a + b - 2c\right)HCO_3^- + \left(\frac{1}{2}a\right)HS^- +$$
$$(b)NH_4^+ + (c)HPO_4^{2-} + \left(\frac{1}{2}a - b + 2c\right)CO_2 + \left(\frac{1}{2}a - b + 2c\right)H_2O, \quad (4)$$

where a, b, and c represent the stoichiometry of the organic matter composition (i.e., in the model runs, the well-known Redfield ratio a:b:c = 106:16:1 is assumed).

The respective Monod-type kinetic rate law is:

$$R_{SO4} = \frac{1-\phi}{\phi} f_i k_G [C_{org}] \frac{[SO_4^{2-}]}{K_{SO4} + [SO_4^{2-}]}, \quad (5)$$

where

k_G = kinetic rate constant for OM degradation,
$[C_{org}]$ = concentration of OM,
$[SO_4^{2-}]$ = concentration of sulfate,
K_{SO4} = Monod constant for sulfate, and
f_i = stoichiometric factor of the respective pore water constituent i (e.g., for SO_4^{2-}: $f = -½$).

Assuming a steady-state distribution for organic matter, the following analytical solution was least-squares fitted to the data and prescribed in the numerical model:

$$[C_{org}] = [C_{org}]_\infty + ([C_{org}]_0 - [C_{org}]_\infty)e^{-\alpha x}, \quad (6)$$

where

$[C_{org}]_0$ = concentration at the sediment surface (i.e., 2.5 wt%),
$[C_{org}]_\infty$ = concentration at the bottom of the sediment column (i.e., 0.2 wt%), and
α = exponential decay constant of the OM distribution (i.e., 2×10^{-4}/cm).

Dirichlet boundary conditions were chosen for the upper and lower boundary in the model scenarios (i.e., the boundary concentrations were fixed to modern bottom seawater values) (Table T2). Because the initial situation (i.e., without influx of seawater sulfate concentration from below) is not known, two extremes were analyzed: (1) the result of steady-state simulations with a "no gradient" bottom boundary condition (resulting in a sulfate profile decreasing with depth until depletion, matching the sulfate gradient at the surface) and (2) a constant seawater concentration throughout the entire sediment column. The details of this sensitivity analysis are reported in **"Fluid Flow in the Oceanic Basement,"** p. 9.

Model II: Fluid Flow in Prism Sediments

In addition to vertical fluid flow, which arises from compaction of oceanic sediment during the subduction process, prism sediments also show lateral fluid flow from greater depth through distinct conduits. In the 1-D representation of a transport-reaction model (equation 1), this lateral fluid flow reduces to a simple source/sink term.

I chose propane as a tracer to quantify vertical and horizontal fluid flow. Because it is inert to biogeochemical reactions in the zones of lat-

eral fluid flow in the prism sediments, mathematically it can be treated independently from other sediment and pore water constituents. Zero concentration boundary and initial conditions were chosen. The porosity equation (equation 2) was fitted separately to the data in the prism and underthrust sediments. This way, the porosity profile, prescribed in the model, correctly resembles the abrupt change across the décollement (Fig. F6).

I collected gas samples for the propane data presented in Figure F7 on board the *JOIDES Resolution* during Leg 205 using the ODP piercing tool (Morris, Villinger, Klaus, et al., 2003). Concentrations are given in parts per million by volume (ppmv) of the sampled gas volume (50 cm^3) because the piercing technique does not allow correlation to the volume of bulk sediment or pore water. N_2 and O_2 concentrations indicated contamination with air, due to core handling, of <10%. Thus, the relative propane profile is quite accurate. The headspace technique does not allow for accurate relative profiles for a number of reasons; most importantly, gas loss prior to sampling is impossible to assess. Hence, I preferred the piercing tool data over the headspace data for numerical analysis. In addition, the piercing tool samples were collected at a higher frequency (three per 10-m core interval) than pore water samples were taken (one per core interval), providing a high-resolution propane profile. However, in Fig. F5 the headspace propane data is shown because during Leg 170 the piercing tool was not used.

F6. AMO reaction front, p. 23.

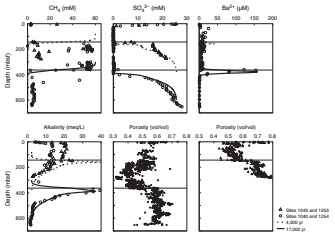

F7. Lateral fluid flow and upward advection, p. 24.

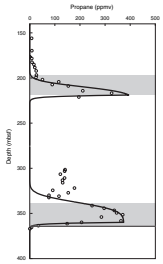

Model III: AMO Reaction Front across the Décollement

The most prominent diagenetic reaction at the décollement is oxidation of the methane-rich pore fluids of the prism wedge by the sulfate-rich pore waters of the subducting oceanic sediments:

$$CH_4 + SO_4^{2-} \rightarrow HCO_3^- + HS^- + H_2O. \quad (7)$$

Mathematically, AMO can be described with a second-order rate law:

$$R_{AMO} = k_{AMO}[CH_4][SO_4^{2-}], \quad (8)$$

where

k_{AMO} = rate constant for AMO,
$[CH_4]$ = methane concentration, and
$[SO_4^{2-}]$ = sulfate concentration.

As SO_4^{2-} becomes depleted in the underthrust sediments, the thermodynamic dissolution of barite is induced, thereby releasing barium into the pore water. In the model, I chose to release barium at a constant rate, R_{Ba}, if the pore water became undersaturated with respect to barite, that is,

$$[Ba^{2+}][SO_4^{2-}] < K_{barite}, \quad (9)$$

where K_{barite} is the solubility product of barite at given pressure, temperature, and salinity conditions.

The numerical model simulates the downward progression of this reaction front in the pore water while the oceanic plate is subducted. Because I am only modeling the depth dimension in space, I cannot simulate the lateral subduction movement itself. In the model, there-

fore, the base of the décollement zone is set to 364.2 mbsf at Site 1254 (Morris, Villinger, Klaus, et al., 2003). For Site 1043/1255, the décollement is located at 144 mbsf. To facilitate comparison, the model results are presented on the same plots (Fig. F6).

The initial conditions of the pore water constituents were approximated by their profiles in the prism and underthrust sediments. Dirichlet boundary conditions were applied at the upper and lower boundaries. The near-surface gradients and reactions of methane and sulfate in the prism sediments were ignored because the scope of this simulation is the reaction front across the décollement. Within this focus, upper boundary conditions sufficiently represent the diagenetic situation. Because headspace and piercing tool methane measurements do not provide correct in situ values if methane is close to or at saturation with the gas or methane hydrate phase, the methane equilibrium concentration for the prism sediments was calculated theoretically after Tishchenko et al. (2005) and used in the model simulations.

The porosity profile prescribed in the model simulation was fitted to the observed data at Sites 1040 and 1254, including the steplike change across the décollement (see also **"Model II: Fluid Flow in Prism Sediments,"** p. 7). The higher porosities at Sites 1043 and 1255 (Fig. F6) were not considered. Hence, diffusivities are slightly underestimated in this model simulation.

RESULTS AND DISCUSSION

I developed transient 1-D transport-reaction models to analyze the hydrological systems of the Costa Rica subduction zone. The aim was to quantify vertical and horizontal fluid flow as well as the respective time scales of the flow systems in the oceanic crust and the prism wedge. In addition, the AMO reaction front across the boundary between prism and underthrust sediments was simulated to investigate the dynamics in the sedimentary carbon cycle during subduction.

Fluid Flow in the Oceanic Basement

The most obvious geochemical characteristic of sediments on the incoming Cocos plate is the observed reversal of pore water constituents to their respective bottom seawater concentrations at ~400 m sediment depth, just above the first sill complex (Fig. F3). This has been interpreted as the influence of horizontal fluid flow of cold modern seawater in the oceanic crust (Kastner et al., 2000; Kastner and Rudnicki, 2004; Kimura, Silver, Blum, et al., 1997; Silver et al., 2000).

Model Parameterization

Model runs were performed to estimate vertical flux of solutes from the basement aquifer into the overlying oceanic sediments as well as the timescale of this event. Whereas seawater acts as a source or a sink for solutes at the surface as well as at the bottom of the sediment column, sulfate reduction of organic material is the dominating diagenetic reaction within sediments. Hence, SO_4^{2-} is consumed below the sediment surface, whereas NH_4^+, PO_4^{3-}, and alkalinity are produced (Fig. F3). Therefore, the biogeochemical reaction term in equation 1 consists of only one term, the Monod-type rate law for OM degradation utilizing sulfate (equation 5). At Site 1039, the sediments contain >2 wt% or-

ganic matter at the surface and concentrations decrease exponentially to an average of 0.2 wt% below 200 mbsf (Fig. F4). This profile shape was least-squares fitted to the analytical solution of steady-state OM degradation (equation 6) and prescribed in the model runs to reduce computational costs. Finally, upper and lower boundary conditions for sulfate are set to bottom-water concentrations to adequately mimic the two seawater sources.

Two scenarios can explain the observed solute profiles (Fig. F3): (1) upward-directed advection of pore water and (2) purely diffusional transport of solutes from the lateral basement flow into the overlying sediment column. The model results of these two possibilities are discussed below.

First, a sensitivity analysis on the sulfate initial condition was performed because the sulfate distribution prior to establishing the lateral flow system in the crust is unknown but critical to the modeling. The tested initial profiles covered the range from a sediment column fully at seawater concentration to completely sulfate depleted. These tests clearly prove (1) upward advection will only lead to the observed sulfate profile if initial concentrations were lower than today, whereas (2) purely diffusional transport requires the initial concentrations to have been close to seawater values in the entire sediment column. In addition, analysis also revealed that the curved shape of the observed sulfate profile indicates a transient situation. These observations cannot be explained by a steady-state situation. Both scenarios predict steady-state profiles with a linear increase with depth below a near-surface sulfate minimum.

Upward Fluid Flow Scenario

The initial sulfate condition can vary between an almost completely sulfate-free sediment column and an exponentially decaying profile with 27.5 mM at the surface and 14 mM at the bottom. In addition, the rate constant for OM degradation, k_G, was chosen such as to fit the observed near-surface gradient when pore water advection is applied. A k_G of 1.6×10^{-8}/yr sufficiently fits this surface gradient.

Starting from such an initial sulfate distribution and applying the above k_G of 1.6×10^{-8}/yr, an upward advection rate, u_0, of 0.15 cm/yr (i.e., 1500 m/m.y.) for the past 200–240 k.y. will lead to a good fit of the observed sulfate data (solid line; Fig. F4). Thus, the total flux of sulfate into the sediment column from below is

$$F_{SO4} = -\phi_\infty \frac{D_{SO4}}{\theta_\infty^2} \frac{\partial [SO_4^{2-}]_\infty}{\partial x} - \phi_\infty u_\infty [SO_4^{2-}]_\infty, \quad (10)$$

which is equal to 2.79 µmol/(cm² yr). This is equivalent to a total flux of 5586–6703 mol/m² within a time span of 200–240 k.y.

Diffusive Transport Scenario

This scenario requires a sulfate-rich sediment column as initial condition (i.e., a constant concentration of 27.5 mM). In addition, the model suggests a reactive surface fraction of OM in the upper 30 mbsf degrading with a rate constant, k_G, of 2.0×10^{-3}/yr, whereas nonreactive OM is buried below this depth. The combination of anoxic OM degradation and upward diffusing SO_4^{2-} results in a good fit of the observed sulfate data within a predicted time of 1 m.y. (dotted line; Fig. F4).

About 0.025 µmol/(cm² yr) sulfate is diffusing from the basement aquifer into the sediment column, corresponding to a total flux of 249 mol/m² within the modeled time span of 1 m.y.

The diffusion scenario suggests a drastic change in organic matter reactivity that somewhat correlates with the observed change in the sedimentation regime from 30 m/m.y. to 105 m/m.y. about 500 k.y. ago (Kimura, Silver, Blum, et al., 1997), and this model result also indicates that the current situation has lasted for the past 1 m.y. Upward advection from the basement into the overlying sediment column, on the other hand, requires sufficient permeability. The total of ~150 m of gabbroic sill found at both drilling sites, Sites 1039 and 1253, shows an increasing number of fractures with depth (Morris, Villinger, Klaus, et al., 2003). However, these fractures are small, and it is not clear if they can maintain the necessary pressure difference to drive the upward advection.

Unfortunately, the other pore water constituents produced during anoxic organic matter degradation, such as NH_4^+, PO_4^{3-}, and alkalinity, do not clarify either scenario. The results of these variables are highly dependent on the chosen initial profile, and as a consequence I have omitted their presentation here.

Water Budget for Hydrothermal Circulation

Because the lateral flow of seawater in the oceanic basement replenishes the sedimentary pore water with solutes, the resulting vertical sulfate flux must be balanced by the flow of seawater in the crust. Thus, it is possible to provide a minimum estimate of the lateral seawater flow based on the sulfate flux calculations.

In the advection scenario, the sulfate flux is equivalent to a seawater flux of 5905 µmol/(cm² yr) or a volume flux of 1 L/(m² yr) at a minimum lateral flow rate of 0.15 cm/yr. This results in a total water volume flux of 203,117–243,740 L/m² within 200–240 k.y.

The diffusive sulfate flux of the second scenario requires a lateral basement flow of only 52.5 µmol/(cm² yr). This is equivalent to a volume flux of 0.009 L/(m² yr) at a lateral flow rate of 0.001 cm/yr or a total volume flux of 9037 L/m² in 1 m.y.

Silver et al. (2000) estimated that a lateral basement flow of cold seawater at discharge rates of 1–5 m/yr would sufficiently cool the oceanic plate to explain the observed low heat flow data of 12 mW/m². At these high lateral flow rates, therefore, the basement aquifer can easily maintain the required constant sulfate concentration at the interface to the sediment column, also suggesting that most seawater circulating through the oceanic crust is subducted.

Fluid Flow in Prism Sediments

Fluid flow in the prism sediments is primarily driven by sediment compaction during the subduction process and chemical dewatering of minerals at elevated temperatures. The latter reactions occur at ~15–20 km sediment depth (Silver et al., 2000), and fluids are channelled through prism sediments parallel to the décollement by faults and conduits. Hence, these pore fluids show a characteristic geochemical composition: distinct peaks of higher alkanes (Kimura, Silver, Blum, et al., 1997) and lithium (Chan and Kastner, 2000) are observed as well as enrichments in Ca^{2+} and depletions in K^+ (Fig. F5) (Kimura, Silver, Blum, et al., 1997). During Leg 205, I collected piercing tool gas samples at Site

1254 at higher spatial resolution (i.e., three samples per core) (Morris, Villinger, Klaus, et al., 2003). The measured propane data show two major peaks: (1) directly above the décollement at ~360 mbsf and (2) at ~220 m sediment depth (Fig. F7). In addition, the asymmetric shape of these peaks also indicates upward advection of pore water due to compaction of the underthrust sediments during subduction.

Both flow systems were quantified during the numerical model runs. Whereas the vertical advection rate can be parameterized directly, the horizontal fluid flow reduces to a source/sink term in equation 1. Both peaks were treated independently using a constant source rate over a distinct interval representing the flow conduit. Less intense fluid flow between these two peaks led to elevated propane levels without any distinct peaks (see data from Leg 170 in Fig. F5). During Leg 205 this interval was not cored, and it is therefore not considered in the model. Because propane is not produced in the ambient sediment, zero initial and boundary conditions were chosen. Figure F7 depicts the model results with the best fit to the measured propane data.

A constant propane source, R_{prop}, of 22 ppmv/yr reproduced the peak maxima best, whereas the width of the propane peak is indicative of the transient character of both flow systems. The model results suggest that the upper conduit has been active for ~2000 yr and the décollement conduit for ~4000 yr. A thickness of 10 cm was chosen for the conduits as suggested by the stratigraphic results from Leg 205 (Morris, Villinger, Klaus, et al., 2003). However, a sensitivity analysis revealed that fluid flow through, for example, a 10-m-thick conduit combined with a propane rate of 0.22 ppmv/yr leads to an identical profile. Thus, the peak height and width depends on the depth-integrated propane rate, that is,

$$F_{prop} = 2.2 \text{ ppmv m/yr.} \quad (11)$$

My model result suggests fairly continuous lateral fluid flow in the prism sediments over a couple of thousand years. Previous studies have suggested that episodic events rather than a stationary process dominate fluid flow in subduction zones. For the Nankai accretionary complex, for example, Saffer and Bekins (1998) suggested transient dewatering on timescales of 80–160 k.y. resulting from 2.5- to 5-m.y. cycles of pore pressure buildup and drainage. From the scatter of the chloride and ammonium profiles of Site 1040, Hensen and Wallmann (2005) inferred these lateral flow pulses need to be shorter than 10 k.y. Even short fluid pulses caused by, for example, seismic activity (Brown et al., 2005) cannot be excluded either, but they likely do not significantly affect the pore water signals. These short pulses will be levelled out by diffusion and advection.

Based on the 1-D modeling approach, it is difficult to determine lateral flow rate in the conduits because the source/sink term also includes the rate of propane production at depth.

In addition, an upward advection rate of 0.4 cm/yr was necessary to properly reproduce the asymmetry of both peaks. This value is in good agreement with the pore water flow resulting from the compaction of the underthrust sediments (i.e., the 25% reduction in overall thickness) (Kimura, Silver, Blum, et al., 1997). This is equivalent to an advection rate of 0.55 cm/yr. Screaton and Saffer (2005) discussed that the hemipelagic sediments dewater vertically, whereas the pelagic carbonate-rich section dewaters parallel to the décollement. However, the 29% reduction of the sediment Units U1 and U2 (Fig. F2) would still contribute to

an advection rate of 0.26 cm/yr, a value close to my result. Hensen and Wallmann (2005) modeled the gas hydrate distribution in the prism sediments and determined a much lower, but steady-state, advection rate (0.03 cm/yr) when simulating the steep sulfate gradient near the sediment/water interface.

Reaction Front across the Décollement

On subduction of the oceanic sediments, these sulfate-rich pore waters come into contact with the completely sulfate-depleted, methane-rich sediments of the prism wedge. As a consequence, a reaction front of AMO develops across the décollement. Whereas close to the deformation front (Sites 1043/1255) the sulfate/methane boundary is still very close to the décollement, the reaction front has already moved ~20 m into the underthrust sediments at Sites 1040/1254 (1.5 km further arcward) (Kimura, Silver, Blum, et al., 1997; Morris, Villinger, Klaus, et al., 2003). Figure F6 depicts the downward progressing reaction front combining data from ODP sites in a graph. A horizontal black line indicates the respective depths of the décollement.

A combination of the following three factors explains the downward progression of the AMO reaction front: (1) porosity values are 10%–15% higher in the underthrust sediments than in the overlying prism sediments (Fig. F6), thus facilitating downward transport of solutes, (2) methane diffusivity is ~60% higher than that of sulfate, and (3) the methane flux from the gas hydrate reservoir and microbial production is potentially larger than the upward-directed replenishment of sulfate from the basement aquifer.

The third numerical transport-reaction model was developed to simulate the downward-progressing AMO reaction front. Because the subduction process cannot be modeled in a 1-D model, the sediment depth is treated relative to the lithologic boundary (represented by the horizontal black lines in Fig. F6). The upper boundary of methane was set to 60 mM, the theoretical equilibrium concentration with the hydrate phase at 300 mbsf, and the measured CH_4 concentrations were normalized to this value. Initially, concentrations above the décollement were set to 60 mM, whereas they were set to zero in the underthrust sediments. In contrast, sulfate concentrations were set to zero in the prism wedge, whereas the observed profile at Site 1039 was prescribed below the décollement. Additionally, porosity distribution at Site 1040, including the step-like change across the décollement, was used in the model calculations.

An AMO rate constant k_{AMO} of 1×10^3/(mM yr) is sufficient to reproduce the measured sulfate data ~1500 m arcward of the deformation front at Sites 1040/1254 (solid lines and open circles, Fig. F6). At a subduction rate of 88 mm/yr (Kimura, Silver, Blum, et al., 1997), this takes 17,000 yr. Thus, 7.4 µmol/(cm² yr) of methane are oxidized by AMO, or a total amount of 1262 mol/m². This is equivalent to ~15 kg of carbon per square meter in 17 k.y. These are minimum values because the methane gradient decreases with time as the AMO front continues to progress deeper. For Sites 1043/1255, closer to the deformation front, the respective rates are 23.9 µmol/(cm² yr) of methane oxidized or 12.9 kg of carbon per square meter after 4.5 k.y. AMO (equation 7) also produces hydrogen sulfide and bicarbonate, as indicated by the alkalinity peak below the décollement (Fig. F6). The model profile fits the observed alkalinity data without any further need to adjust, suggesting an

appropriate model formulation. In addition, as SO_4^{2-} becomes depleted in the underthrust sediments, barite starts to dissolve, thereby releasing barium and sulfate into the pore water (Fig. F6). The numerical model determines a barite dissolution rate of 1.2×10^{-5} mM/yr, which is equivalent to a Ba^{2+} flux of 23.6 µmol/(cm² yr). Hence, a total amount of 130 kg of sulfur per square meter was dissolved within 17 k.y.

The model parameters (i.e., the AMO rate constant and barite dissolution rate) were adjusted solely to match the observed profiles at Sites 1040/1254. This parameterization was then used to successfully reproduce pore water distributions after 4500 yr of subduction at the drilling sites closer to the deformation front (i.e., Sites 1043/1255) without any further model adjustments. However, geochemical fluxes during these first 4500 yr of subduction are slightly underestimated because I used the porosity distribution of Sites 1040/1254 in this model run.

SUMMARY AND CONCLUSIONS

This study investigated the hydrological system of the Costa Rica subduction zone based on data from Legs 170 and 205. In detail, 1-D numerical transport-reaction models were developed to quantify the geochemical fluxes and timescales associated with (1) the flow of cold modern seawater in the basement and (2) fluid flow in the sediments of the prism wedge. The latter fluid flow has two sources: vertical dewatering of the compacted underthrust sediments and lateral flow along conduits parallel to the décollement with thermogenic origin.

Finally, the main results of this study can be summarized as follows:

1. Only a small fraction of the cold seawater circulating in the oceanic basement is released through the overlying sediment, either by advection or diffusion. Thus, most of this water will be subducted.
2. Based on the sulfate profile of the oceanic sediments, the basement aquifer has been active for the past 240 k.y. to 1 m.y., depending on the respective transport process.
3. The propane profile in the prism wedge suggests vertical dewatering due to compaction across the décollement as well as deep-sourced fluid flow along and parallel to the décollement.
4. Lateral fluid flow in the prism sediments is not a steady-state process. The current flow pulse in the upper conduit and the décollement zone has been active for 2000 and 4000 yr, respectively.
5. Short-term pulses on the order of weeks or months, resulting from seismic activity, likely do not have significant impacts on the overall fluid expulsion.
6. The AMO reaction front between the prism and underthrust sediments remobilizes considerable amounts of sulfur, and potentially the methane demand will even lead to the decomposition of gas hydrates above the décollement.

ACKNOWLEDGMENTS

I would like to thank the crew and technical staff of the *JOIDES Resolution* for their help in collecting and analyzing the data during Leg 205. I greatly enjoyed the many helpful and enlightening discussions with

M. Kastner and the Leg 205 Shipboard Scientific Party. I would also like to acknowledge the two reviewers, I. L'Heureux and A. Dale, for their constructive comments. Finally, I would like to express my gratitude to CanadaODP for supporting my cruise participation and for reimbursing the travel expenses. M. Haeckel was supported by the Alexander von Humboldt Foundation, Germany. This research used samples and/or data provided by the Ocean Drilling Program (ODP). ODP is sponsored by the U.S. National Science Foundation (NSF) and participating countries under management of Joint Oceanographic Institutions (JOI), Inc.

REFERENCES

Baker, P.A., Stout, P.M., Kastner, M., and Elderfield, H., 1991. Large-scale lateral advection of seawater through oceanic crust in the central equatorial Pacific. *Earth Planet. Sci. Lett.,* 105(4):522–533. **doi:10.1016/0012-821X(91)90189-O**

Bekins, B.A., McCaffrey, A.M., and Driess, S.J., 1995. Episodic and constant flow models for the origin of low-chloride waters in a modern accretionary complex. *Water Resour. Res.,* 31(12):3205–3216. **doi:10.1029/95WR02569**

Berner, R.A., 1980. *Early Diagenesis: A Theoretical Approach:* Princeton, NJ (Princeton Univ. Press).

Boudreau, B.P., 1996. A method-of-lines code for carbon and nutrient diagenesis in aquatic sediments. *Comp. Geosci.,* 22(5):479–496. **doi:10.1016/0098-3004(95)00115-8**

Boudreau, B.P., 1997. *Diagenetic Models and Their Implementation: Modelling Transport and Reactions in Aquatic Sediments:* Berlin, Heidelberg, New York (Springer-Verlag).

Brown, K.M., Tryon, M.D., DeShon, H.R., Dorman, L.M., and Schwartz, S.Y., 2005. Correlated transient fluid pulsing and seismic tremor in the Costa Rica subduction zone. *Earth Planet. Sci. Lett.,* 238(1–2):189–203. **doi:10.1016/j.epsl.2005.06.055**

Chan, L.-H., and Kastner, M., 2000. Lithium isotopic compositions of pore fluids and sediments in the Costa Rica subduction zone: implications for fluid processes and sediment contribution to the arc volcanoes. *Earth Planet. Sci. Lett.,* 183(1–2):275–290. **doi:10.1016/S0012-821X(00)00275-2**

Claypool, G.E., and Kvenvolden, K.A., 1983. Methane and other hydrocarbon gases in marine sediment. *Annu. Rev. Earth Planet. Sci.,* 11(1):299–327. **doi:10.1146/annurev.ea.11.050183.001503**

Fisher, A.T., and Becker, K., 2000. Channelized fluid flow in oceanic crust reconciles heat-flow and permeability data. *Nature (London, U. K.),* 403(6765):71–74. **doi:10.1038/47463**

Fisher, A.T., Davis, E.E., Hutnak, M., Spiess, V., Zühlsdorff, L., Cherkaoui, A., Christiansen, L., Edwards, K., Macdonald, R., Villinger, H., Mottl, M.J., Wheat, C.G., and Becker, K., 2003. Hydrothermal recharge and discharge across 50 km guided by seamounts on a young ridge flank. *Nature (London, U. K.),* 421:618–621. **doi:10.1038/nature01352**

Giambalvo, E.R., Steefel, C.I., Fisher, A.T., Rosenberg, N.D., and Wheat, C.G., 2002. Effect of fluid-sediment reaction on hydrothermal fluxes of major elements, eastern flank of the Juan de Fuca Ridge. *Geochim. Cosmochim. Acta,* 66(10):1739–1757. **doi:10.1016/S0016-7037(01)00878-X**

Hensen, C., and Wallmann, K., 2005. Methane formation at Costa Rica continental margin—constraints for gas hydrate inventories and cross-décollement fluid flow. *Earth Planet. Sci. Lett.,* 236(1–2):41–60. **doi:10.1016/j.epsl.2005.06.007**

Kastner, M., Elderfield, H., and Martin, J.B., 1991. Fluids in convergent margins: what do we know about their composition, origin, role in diagenesis and importance for oceanic chemical fluxes? *Philos. Trans. R. Soc. London, Ser. A,* 335:243–259.

Kastner, M., Morris, J., Chan, L.H., Saether, O., and Luckge, A., 2000. Three distinct fluid systems at the Costa Rica subduction zone: chemistry, hydrology, and fluxes. *Goldschmidt 2000, J. Conf. Abstr.,* 5:572. (Abstract)

Kastner, M., and Rudnicki, M.D., 2004. Ridge flank sediment-fluid interactions. *In* Davis, E., and Elderfield, H. (Eds.), *Hydrogeology of the Oceanic Lithosphere:* Cambridge (Cambridge Univ. Press), 534–571.

Kimura, G., Silver, E.A., Blum, P., et al., 1997. *Proc. ODP, Init. Repts.,* 170: College Station, TX (Ocean Drilling Program). [**HTML**]

Langseth, M.G., and Silver, E.A., 1996. The Nicoya convergent margin: a region of exceptionally low heat flow. *Geophys. Res. Lett.,* 23:891–894.

Li, Y., and Gregory, S., 1974. Diffusion of ions in sea water and in deep-sea sediments. *Geochim. Cosmochim. Acta,* 38:703–714.

Morris, J.D., Leeman, W.P., and Tera, F., 1990. The subducted component in island arc lavas: constraints from Be isotopes and B-Be systematics. *Nature (London, U. K.),* 344:31–36.

Morris, J., Valentine, R., and Harrison, T., 2002. ^{10}Be imaging of sediment accretion, subduction along the northeast Japan and Costa Rica convergent margins. *Geology,* 30(1):59–62. **doi:10.1130/0091-7613(2002)030<0059:BIOSAA>2.0.CO;2**

Morris, J.D., Villinger, H.W., Klaus, A., et al., 2003. *Proc. ODP, Init. Repts.,* 205 [CD-ROM]. Available from: Ocean Drilling Program, Texas A&M University, College Station TX 77845-9547, USA. [**HTML**]

Ranero, C.R., and von Huene, R., 2000. Subduction erosion along the Middle America convergent margin. *Nature (London, U. K.),* 404(6779):748–752. **doi:10.1038/35008046**

Richter, F.M., 1993. Fluid flow in deep-sea carbonates: estimates based on porewater Sr. *Earth Planet. Sci. Lett.,* 119(1–2):133–141. **doi:10.1016/0012-821X(93)90011-W**

Richter, F.M., 1996. Models for the coupled Sr-sulfate budget in deep-sea carbonates. *Earth Planet. Sci. Lett.,* 141:199–212.

Rudnicki, M.D., Elderfield, H., and Mottl, M.J., 2001. Pore fluid advection and reaction in sediments of the eastern flank, Juan de Fuca Ridge, 48°N. *Earth Planet. Sci. Lett.,* 187(1–2):173–189. **doi:10.1016/S0012-821X(01)00287-4**

Rüpke, L.H., Morgan, J.P., Hort, M., and Connolly, J.A.D., 2002. Are the regional variations in Central American arc lavas due to differing basaltic versus peridotitic slab sources of fluids? *Geology,* 30(11):1035–1038. **doi:10.1130/0091-7613(2002)030<1035:ATRVIC>2.0.CO;2**

Saffer, D.M., and Bekins, B.A., 1998. Episodic fluid flow in the Nankai accretionary complex: timescale, geochemistry, flow rates, and fluid budget. *J. Geophys. Res.,* 103(B12):30351–30371. **doi:10.1029/98JB01983**

Saffer, D.M., and Bekins, B.A., 1999. Fluid budgets at convergent plate margins: implications for the extent and duration of fault-zone dilation. *Geology,* 27(12):1095–1098. **doi:10.1130/0091-7613(1999)027<1095:FBACPM>2.3.CO;2**

Screaton, E.J., and Saffer, D.M., 2005. Fluid expulsion and overpressure development during initial subduction at the Costa Rica convergent margin. *Earth Planet. Sci. Lett.,* 233(3–4):361–374. **doi:10.1016/j.epsl.2005.02.017**

Silver, E., Fisher, A., Saffer, D., Kastner, M., Morris, J., and McIntosh, K., 2000. Fluid flow paths in the Middle America Trench and Costa Rica margin. *Geology,* 28(8):679–682. **doi:10.1130/0091-7613(2000)028<0679:FFPITM>2.3.CO;2**

Stumm, W., and Morgan, J.J., 1996. *Aquatic Chemistry: Chemical Equilibria and Rates in Natural Waters* (3rd ed.): New York (Wiley).

Tishchenko, P., Hensen, C., Wallmann, K., and Wong, C.S., 2005. Calculation of the stability and solubility of methane hydrate in seawater. *Chem. Geol.,* 219(1–4):37–52. **doi:10.1016/j.chemgeo.2005.02.008**

Vannucchi, P., Ranero, C.R., Galeotti, S., Straub, S.M., Scholl, D.W., and McDougall-Ried, K., 2003. Fast rates of subduction erosion along the Costa Rica Pacific margin: implications for nonsteady rates of crustal recycling at subduction zones. *J. Geophys. Res.,* 108(B11):2511. **doi:10.1029/2002JB002207**

You, C.-F., Castillo, P.R., Gieskes, J.M., Chan, L.H., and Spivack, A.J., 1996. Trace element behavior in hydrothermal experiments: implications for fluid processes in subduction zones. *Earth Planet Sci. Lett.,* 140(1–4):41–52. **doi:10.1016/0012-821X(96)00049-0**

Figure F1. A. Map of drilling locations of Legs 170 and 205 offshore Nicoya Peninsula, Costa Rica. **B.** Projection of drilling sites and total drilling depths onto a migrated multichannel seismic profile across the Middle America Trench (Line BGR-99-44; modified from Morris, Villinger, Klaus, et al., 2003). Leg 205 sites are shown in black and Leg 170 sites are shown in gray.

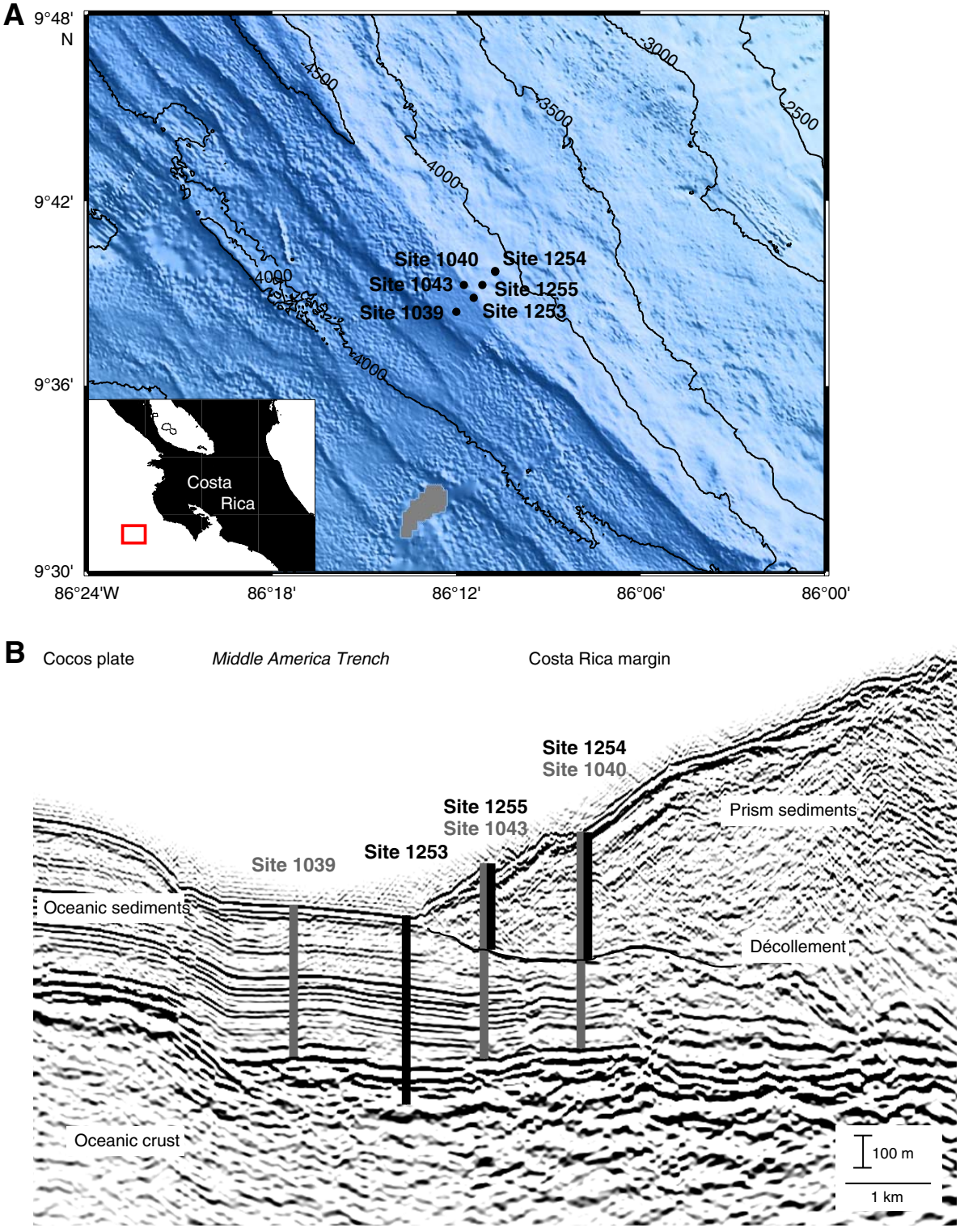

Figure F2. Simplified lithology of cores drilled during Legs 170 (Kimura, Silver, Blum, et al., 1997) and 205 (Morris, Villinger, Klaus, et al., 2003). Depths of lithological units reflect findings of Leg 205 (i.e., respective depths found in the drill holes of Leg 170 differ slightly). Units U1 and U2 = siliceous hemipelagic sediment section, U3 = carbonate-rich pelagic section, U4 = gabbroic sill of the incoming and subducting oceanic plate. Unit P1 = prism sediments.

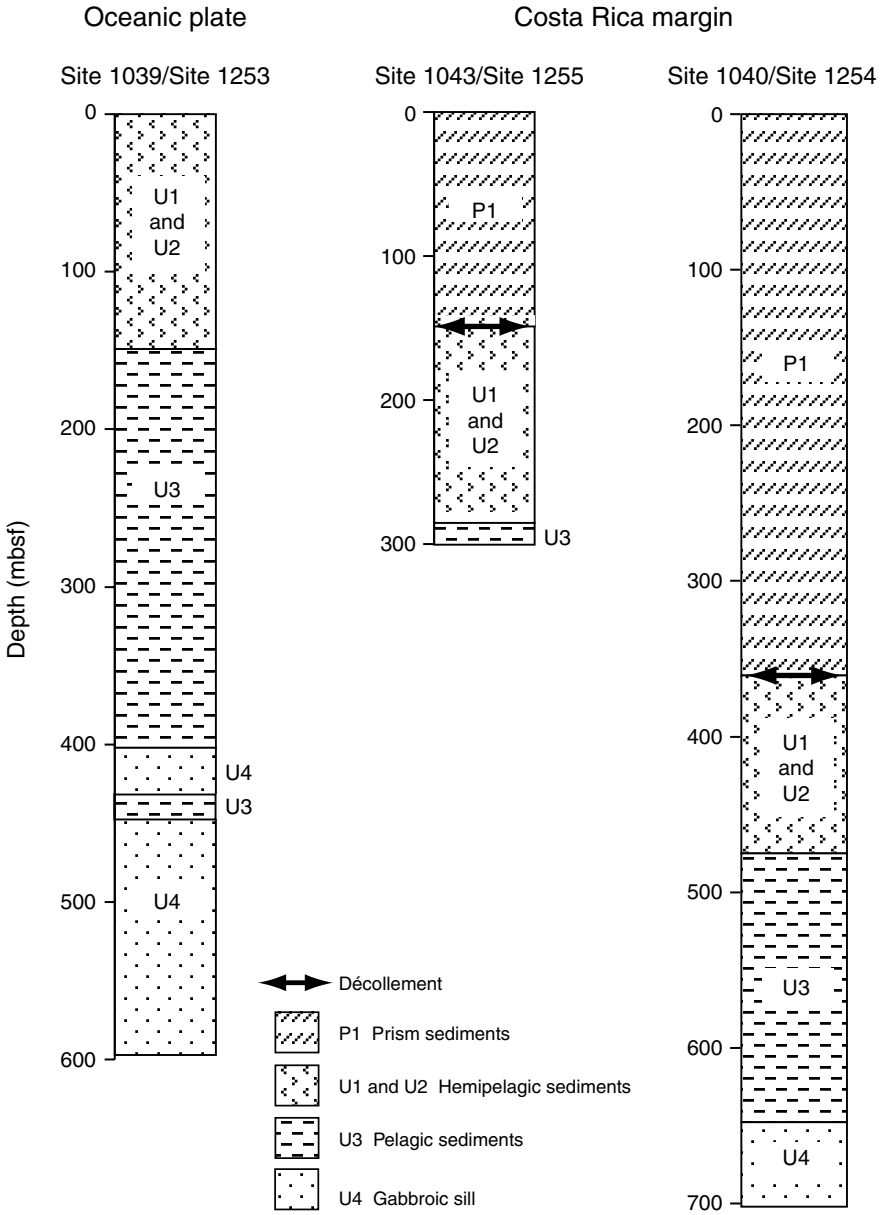

Figure F3. Geochemical data in sediments of the oceanic plate. Gray areas = sections of igneous rock (gabbroic sill) recovered during Leg 205.

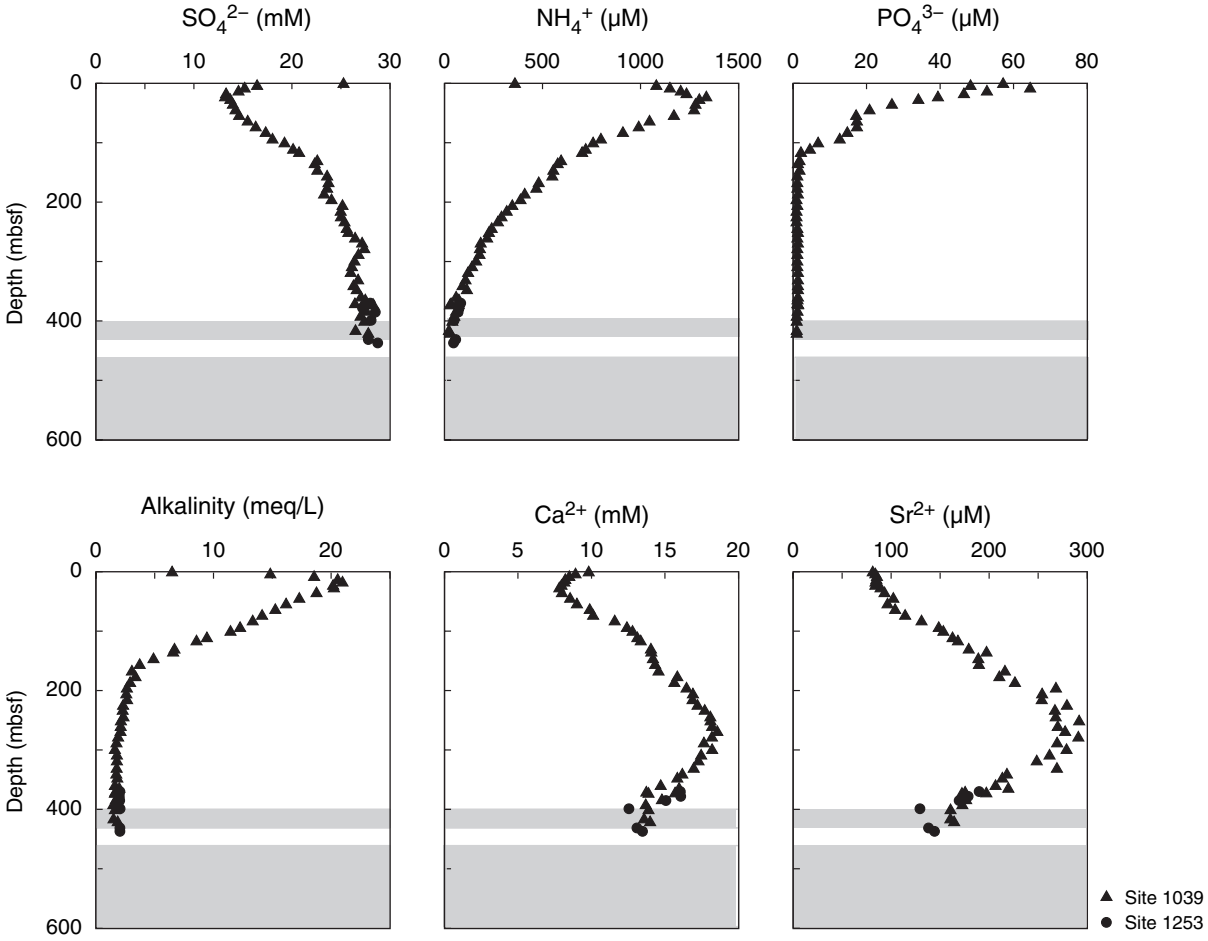

Figure F4. Results of numerical non-steady-state simulations reproducing sulfate pore water data of Sites 1039 and 1253. Solid line = numerical simulation including upward advection of fluids, dashed line = purely diffusional transport of pore water components. Gray areas = depth of upper sill recovered during Leg 205.

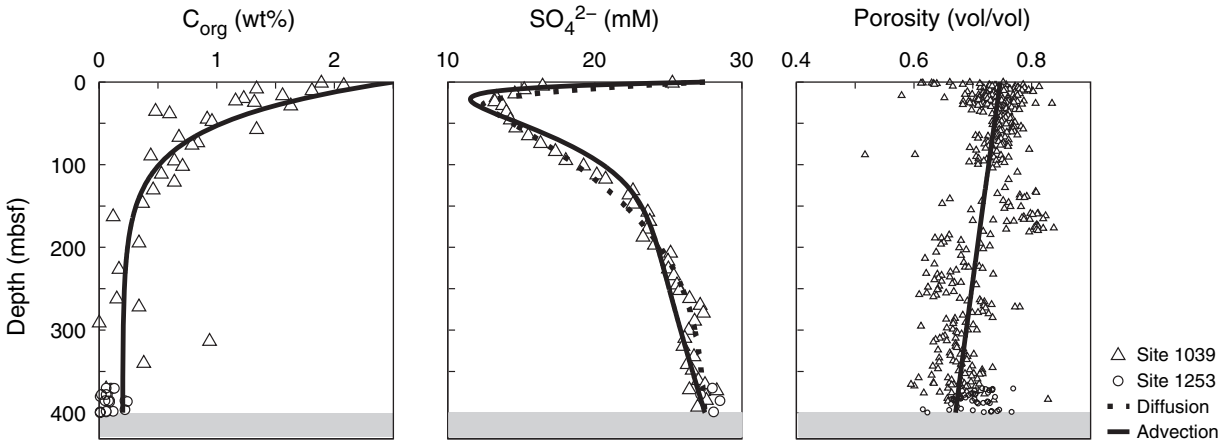

Figure F5. Pore water data of prism and underthrust sediments indicating lateral fluid flow along the décollement and an upper flow conduit (gray shaded areas). **A.** Sites 1040 and Site 1254 1.5 km arcward of the deformation front. **B.** Sites 1043 and 1255 0.4 km arcward of the deformation front. Note that propane data shown here were determined using the headspace sampling technique.

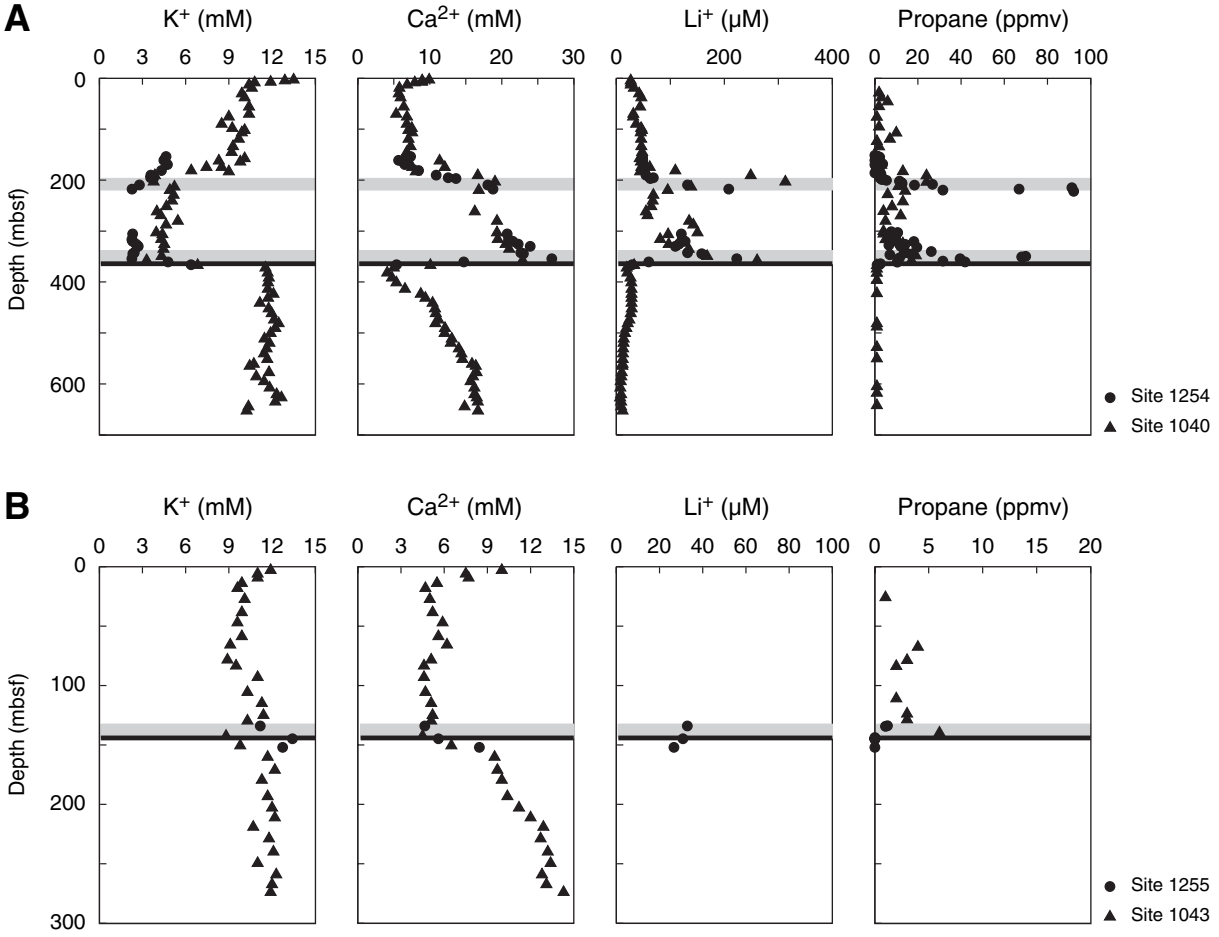

Figure F6. Slowly progressing reaction front of AMO across the décollement. Comparison of numerical simulations after 4,500 yr and 17,000 yr and combined pore water data for Sites 1043, 1040, 1254, and 1255. Horizontal black lines = décollement at Sites 1043/1255 (close to the deformation front) and Sites 1040/1254 (further arcward of the deformation front), reflecting the subduction process of the oceanic plate.

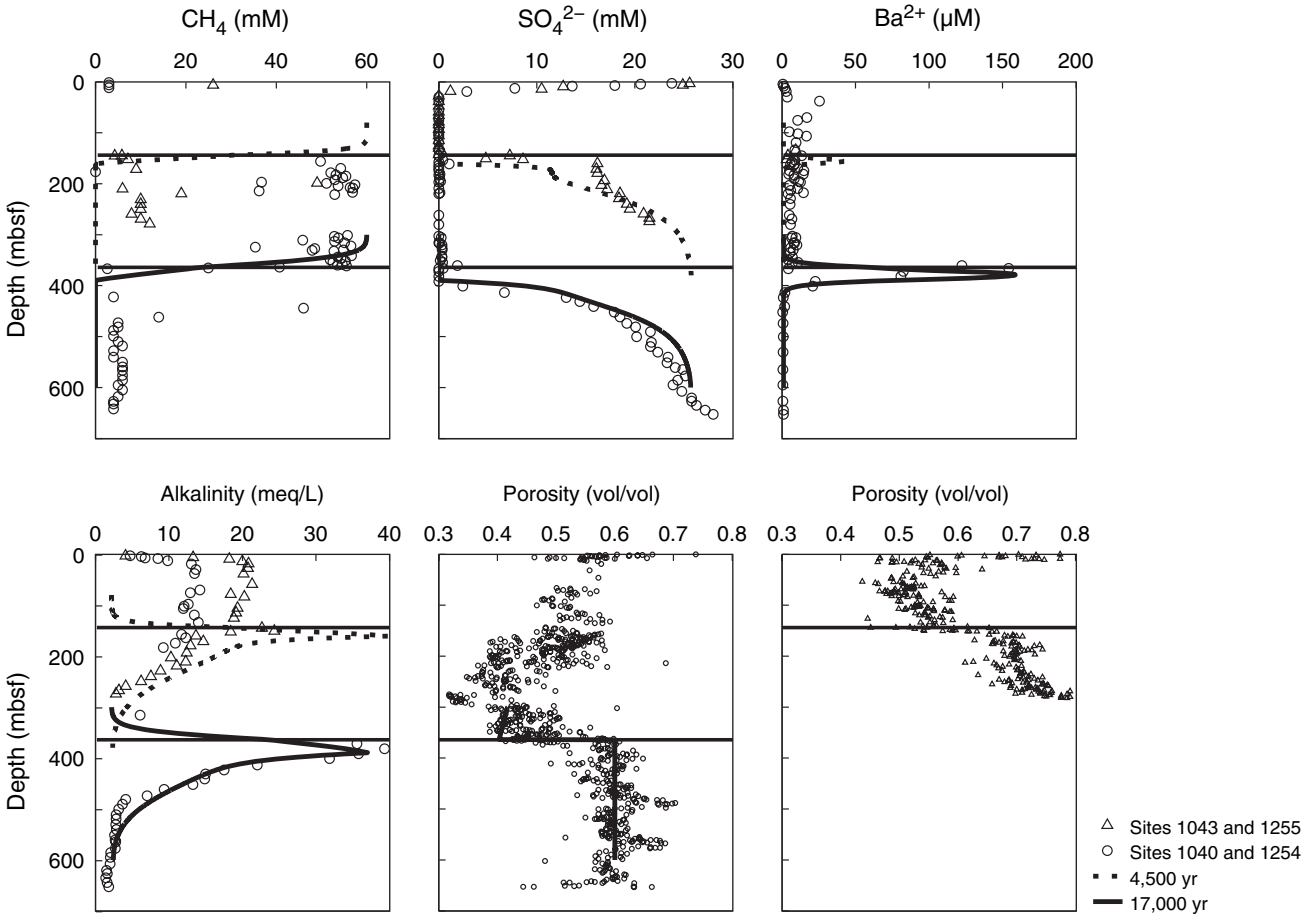

Figure F7. Results from non-steady-state model simulating lateral fluid flow along flow conduits (gray shaded areas) in the prism sediments as well as upward advection due to compaction of the subducting oceanic sediments. Propane data (circles) were collected on Leg 205 using the ODP piercing tool. Line at 360.6 mbsf = lithologic boundary.

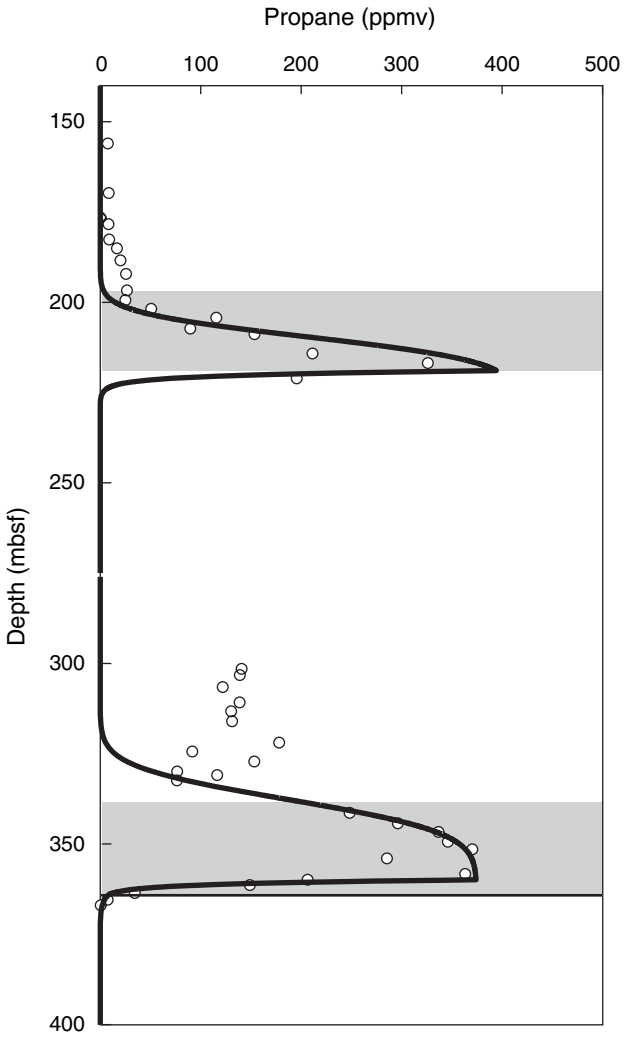

Table T1. Location of drill sites and holes, Legs 170 and 205.

Site, hole	Latitude	Longitude	Water depth (m)	Cored interval (m)
170-				
1039B	9°38.405′N	86°12.003′E	4364.5	0.0–384.3
1039C	9°38.383′N	86°12.002′E	4362.2	363.1–448.7
1040B	9°39.707′N	86°10.746′E	4189.0	0.0–190.2
1040C	9°39.697′N	86°10.735′E	4189.0	159.3–665.0
1042A	9°39.273′N	86°11.160′E	4324.0	0.0–282.3
205-				
1253A	9°38.8583′N	86°11.4337′E	4376.3	370.0–600.0
1254A	9°39.6989′N	86°10.7435′E	4182.8	150.0–223.0, 300.0–367.5
1255A	9°39.2716′N	86°11.1492′E	4311.6	123.0–157.0

Table T2. Parameters and boundary conditions for the three numerical model setups.

Parameter	Model I	Model II	Model III
Depth of calculation x_{top}–x_{bottom}	0–400 m	100–500 m	300–600 m
Water depth	4376.3 m	4182.8 m	4311.6 m
Water temperature	2°C	2°C	2°C
Salinity	34.5	34.5	34.5
Sedimentation rate ω_∞	4.1 cm/k.y.	NA	NA
Advection rate u_0 (vertical fluid flow scenario)*	0.15 cm/yr	0.4 cm/yr	0.4 cm/yr
Advection rate u_0 (pure diffusion scenario)*	0.0 cm/yr	NA	NA
Porosity at sediment surface ϕ_0	0.747	0.592	0.592
Porosity at infinity ϕ_∞	0	0.364	0.364
Porosity attenuation coefficient β	2.69×10^{-6}/cm	4.83×10^{-5}/cm	4.83×10^{-5}/cm
$[SO_4^{2-}]$ (x_{top}, t)	27.5 mM	NA	27.5 mM
$[SO_4^{2-}]$ (x_{bottom}, t)	27.5 mM	NA	27.5 mM
$[C_3H_8]$ (x_{top}, t)	NA	0 ppmv	NA
$[C_3H_8]$ (x_{bottom}, t)	NA	0 ppmv	NA
$[CH_4]$ (x_{top}, t)	NA	NA	60 mM
$[CH_4]$ (x_{bottom}, t)	NA	NA	0 mM
$[HS^-]$ (x_{top}, t)	0 mM	NA	0 mM
$[HS^-]$ (x_{bottom}, t)	0 mM	NA	0 mM
$[HCO_3^-]$ (x_{top}, t)	2.2 mM	NA	2.2 mM
$[HCO_3^-]$ (x_{bottom}, t)	2.2 mM	NA	2.2 mM
$[Ba^{2+}]$(x_{top}, t)	NA	NA	0 mM
$d[Ba^{2+}]/dx$ (x_{bottom}, t)	NA	NA	0 mM/cm
Rate constant for OM degradation k_{G0} (vertical fluid flow scenario)*	1.6×10^{-8}/yr	NA	NA
Rate constant for OM degradation k_{G0} (pure diffusion scenario)*	2.0×10^{-3}/yr	NA	NA
Monod constant for SO_4^{2-} K_{SO4}	1 mM	NA	NA
Rate for propane source R_{prop}*	NA	22 ppmv/yr	NA
Barite solubility constant K_{barite}	NA	NA	3.72×10^{-5}/mM^2
Rate for barite dissolution R_{Ba}*	NA	NA	1.2×10^{-5} mM/yr
Rate constant for AMO k_{AMO}*	NA	NA	1×10^3/(mM yr)

Notes: NA = not applicable. * = parameter adjusted in model runs. Below the décollement, the porosity is set to a constant value of 0.6 to match observed data. Model I Monod constant from Boudreau (1996). Model III Barite solubility constant from Stumm and Morgan (1996).